Title

Structural and biological studies on bacterial nitric oxide synthase inhibitors.

Journal

Proceedings of the National Academy of Sciences of the United States of America, 110(45)

Authors

Holden, Jeffrey
Jing, Qing
Kang, Soosung
et al.

Publication Date

2013-11-05

DOI

10.1073/pnas.1314080110

Peer reviewed

Structural and biological studies on bacterial nitric oxide synthase inhibitors

Jeffrey K. Holden[a], Huiying Li[a], Qing Jing[b], Soosung Kang[b], Jerry Richo[a], Richard B. Silverman[b,1], and Thomas L. Poulos[b,1]

[a]Departments of Molecular Biology and Biochemistry, Pharmaceutical Sciences, and Chemistry, University of California, Irvine, CA 92697-3900; and [b]Departments of Chemistry and Molecular Biosciences, Chemistry of Life Processes Institute, Center for Molecular Innovation and Drug Discovery, Northwestern University, Evanston, IL 60208-3113

Edited by Douglas C. Rees, Howard Hughes Medical Institute, California Institute of Technology, Pasadena, CA, and approved September 23, 2013 (received for review July 29, 2013)

Nitric oxide (NO) produced by bacterial NOS functions as a cytoprotective agent against oxidative stress in *Staphylococcus aureus*, *Bacillus anthracis,* and *Bacillus subtilis*. The screening of several NOS-selective inhibitors uncovered two inhibitors with potential antimicrobial properties. These two compounds impede the growth of *B. subtilis* under oxidative stress, and crystal structures show that each compound exhibits a unique binding mode. Both compounds serve as excellent leads for the future development of antimicrobials against bacterial NOS-containing bacteria.

crystallography | antibiotics

NO is a highly reactive free radical produced by the hemethiolate monooxygenase nitric oxide synthase (NOS). NOS generates NO by oxidizing L-Arg and is found in both mammals and some bacteria. Mammalian NOS (mNOS) is a multidomain protein composed of both oxygenase and reductase domains, whereas bacterial NOS (bNOS) from the genus *Bacillus* and *Staphylococcus* contains only an oxygenase domain. X-ray crystal structures determined for both bNOS and mNOS oxygenase domains reveals a near-identical tertiary structure and active site except that bNOS lacks the N-terminal fragment that contains the Zn^{2+} binding motif observed in mNOS (1).

In mammalian systems, NO functions as an essential signaling molecule and is involved in a variety of physiological functions ranging from blood pressure homeostasis to neural cell communication and host defense (2). There are three mNOS isoforms: endothelial NOS (eNOS), inducible NOS (iNOS), and neuronal NOS (nNOS). Owing to the pathological consequences of the overproduction or underproduction of NO (3–5), a significant effort has been made toward the development and characterization of isoform selective mNOS inhibitors, which has resulted in the development of many unique inhibitors (6, 7).

In Gram-positive bacteria, bNOS-produced NO has been found to modulate macromolecules by nitrosylation (8, 9), to function as a commensal molecule (10), to protect against oxidative stress (11), and to detoxify antimicrobials (12). Although the biological function of NO varies among bacterial organisms, the unique ability of NO to protect the pathogens *Staphyloccocus aureus* and *Bacillus anthracis* against oxidative and antibiotic-induced oxidative stress (12) by activation of catalase and by suppression of damaging Fenton chemistry (11, 13) implicates bNOS as a potential therapeutic target. Moreover, commonly used antibiotics for the treatment of Gram-positive pathogens—like beta-lactams and vancomycin—elicit antibacterial function by generation of reactive oxygen species (14). Together, these data suggest that inhibition of bNOS will attenuate bacterial survival against antibiotic-induced oxidative stress. Owing to the essential role NO plays in mammals, development of a bNOS-specific inhibitor ideally should take advantage of subtle differences between bNOS and mNOS. To do so first requires identification of NOS inhibitors that demonstrate antimicrobial-like properties within a bacterial system under oxidative stress and characterization of the inhibitor-binding mode for future structure-based inhibitor development. The number of studies on the effects of inhibitors on bNOS has been limited to the finding that nonselective NOS inhibitor N^G-methyl-L-arginine generates greater sensitivity to H_2O_2-induced oxidative stress in *B. anthracis* (13). Here we present results identifying NOS inhibitors that exhibit a dramatic decrease in bacterial viability in the presence of either an antimicrobial agent or H_2O_2 and present spectral and crystallographic studies on the binding of these inhibitors to a *B. subtilis* NOS (bsNOS).

Results and Discussion

Effect of Oxidative Stress and NOS Inhibitor on *B. subtilis*. Bacterial oxidative stress was induced by addition of either H_2O_2 or the antimicrobial agent acriflavine (ACR). Direct comparison of WT and *Δnos B. subtilis* treated with ACR (Fig. 1) revealed the *Δnos B. subtilis* strain to have a decreased percent survival in comparison with the untreated cells, as previously observed (12). To identify NOS inhibitors that enhance the toxicity of oxidative stress on WT *B. subtilis*, we used a library of inhibitors that were designed to target nNOS (6, 7). Initially, we identified inhibitors that bound the bsNOS active site based on an imidazole displacement analysis outlined in *Materials and Methods*. From the NOS inhibitors identified to bind bsNOS, we then screened 10 NOS inhibitors (*SI Appendix*, Table S1) for the ability to delay *B. subtilis* growth in the presence of oxidative stress. From our initial screen, two NOS inhibitors, compounds **1** and **2** (Fig. 2),

Significance

Nitric oxide (NO) produced by bacterial nitric oxide synthase has recently been shown to protect the Gram-positive pathogens *Bacillus anthracis* and *Staphylococcus aureus* from antibiotics and oxidative stress. Using *Bacillus subtilis* as a model system, we identified two NOS inhibitors that work in conjunction with an antibiotic to kill *B. subtilis*. Moreover, comparison of inhibitor-bound crystal structures between the bacterial NOS and mammalian NOS revealed an unprecedented mode of binding to the bacterial NOS that can be further exploited for future structure-based drug design. Overall, this work is an important advance in developing inhibitors against gram-positive pathogens.

Author contributions: J.K.H. designed research; J.K.H. and J.R. performed research; Q.J. and S.K. contributed new reagents/analytic tools; J.K.H., H.L., R.B.S., and T.L.P. analyzed data; and J.K.H., R.B.S., and T.L.P. wrote the paper.

The authors declare no conflict of interest.

This article is a PNAS Direct Submission.

Data deposition: The atomic coordinates and structure factors have been deposited in the Protein Data Bank, www.pdb.org (PDB ID codes 4LWA, 4LWB, 4LUW, and 4LUX).

[1]To whom correspondence may be addressed. E-mail: poulos@uci.edu or Agman@chem.northwestern.edu.

This article contains supporting information online at www.pnas.org/lookup/suppl/doi:10.1073/pnas.1314080110/-/DCSupplemental.

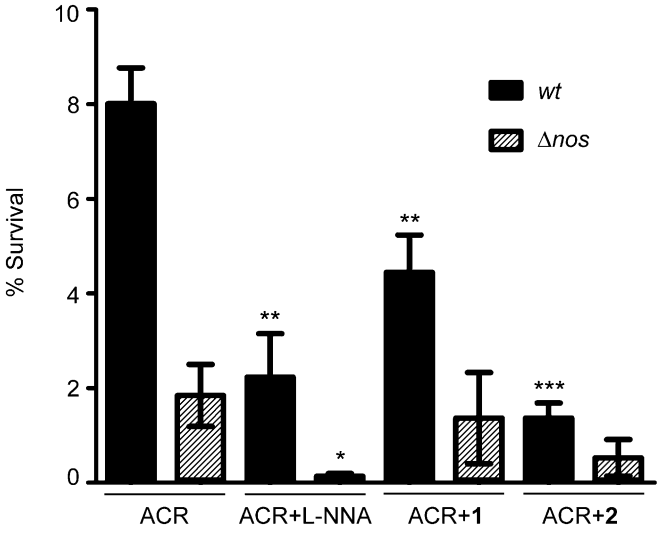

Fig. 1. NOS inhibitors and their effect on *B. subtilis* survival. Bacterial survival of *B. subtilis* WT and *Δnos* strains decreases in the presence of 1.25 mM ACR and NOS inhibitors. The concentrations were 500 μM for L-NNA and **1** and 250 μM for **2**, indicating that **2**+ACR is more effective at inhibiting growth at 250 μM inhibitor than L-NNA+ACR at 500 μM inhibitor. Error bars represent the mean ± the SEM of at least three replicates. Student *t* test gives ***$P < 0.001$, **$P < 0.01$, *$P < 0.05$.

were demonstrated to have antimicrobial-like properties with varying potencies. Further analysis revealed **2** significantly lowers the percent survival of WT ACR (Fig. 1) and WT H_2O_2 treated cells (*SI Appendix*, Fig. S1) and is more potent than **1**. We also tested the nonselective NOS inhibitor L-NNA and found bacterial percent survival to decrease in the presence of ACR (*SI Appendix*, Fig. S1). Interestingly, L-NNA has trivial effects on bacterial survival in the presence of H_2O_2, similar to **1** (*SI Appendix*, Fig. S1).

From the above results, it is clear that NOS inhibitors decrease the percent survival of oxidatively stressed *B. subtilis*. To corroborate the additive effect of oxidative stress with NOS inhibitors on bacterial survival, *B. subtilis* growth was monitored over time in the presence of the antimicrobial agent ACR and/or NOS inhibitor (Fig. 2). Both untreated WT and *Δnos B. subtilis* growth curves revealed nearly identical growth rates. *B. subtilis* strains cocultured with **1** or **2** demonstrated a slightly delayed growth but equal in both WT and *Δnos* cells relative to untreated cells. Most importantly, *Δnos* cells treated with ACR result in a dramatic shift in growth relative to WT treated with ACR. Moreover, cells cotreated with ACR and either **1** or **2** showed a severely delayed growth relative to the ACR treated cell. Compound **2** is the more potent inhibitor because it is more effective at 400 μM than **1** is at 800 μM (Fig. 2).

The effect of the more potent inhibitor, **2**, on *Δnos* suggests **2** to function promiscuously within *B. subtilis*. Based on the WT results (Fig. 2*B*), we might have expected *Δnos* to exhibit the same growth pattern in the presence of ACR alone as WT in the presence of ACR+**2**. This, however, is not the case. ACR does not inhibit *Δnos* growth to the extent one might have expected, and the addition of **2**+ACR has a dramatic effect on growth (Fig. 2*D*). This suggests that **2** may be hitting some other non-NOS target or encouraging ACR-mediated oxidative stress through a currently unknown mechanism. If the former, this hypothetical non-NOS target cannot be very important in WT *B. subtilis* because **1** and **2** have little effect on percent survival (*SI Appendix*, Fig. S1) and bacterial growth (Fig. 2) in the absence of oxidative stress. Therefore, a significant part of the ability of **1** and **2** to block bacterial growth in WT *B. subtilis* is consistent with blocking NO production, which increases the susceptibility to antibiotic-induced oxidative stress (12).

Inhibitor Binding. The imidazole displacement shift from low to high spin was used to estimate the spectral dissociation constant, K_S (15) for bsNOS, eNOS, and nNOS (Table 1 and *SI Appendix*, Fig. S2). Both inhibitors bind to bsNOS with similar affinities to eNOS and nNOS, with **2** being an especially good inhibitor. This correlates well with **2** being especially effective at inhibiting bacterial growth.

Crystal Structures. X-ray data were collected on single crystals soaked in H_4B and NOS inhibitor. bsNOS crystals contain one monomer of bsNOS per asymmetric unit, and the functional dimer is generated by the twofold crystallographic symmetry axis, as previously observed (16). The alpha carbon rmsd between the inhibitor-bound crystal structures and the search model (Protein Data Bank 2FBZ) for residues 2–137 and 147–363 are less then 0.36 Å; residues 138–146 were excluded because of sequence differences between our crystal structures and the search model. On the basis of the low rmsd, we were able to conclude surface mutations E25A/E26A/E316A, selected for reasons outlined in *Materials and Methods*, did not affect the overall structure.

Electron density maps for both **1** and **2** clearly establish that the aminopyridine group is positioned on the distal face of the heme active site to hydrogen-bond with the protein-derived Glu243 residue (Fig. 3 *A* and *B*). In the bsNOS-**1** structure the pyrrolidine ring is positioned within 2.7 Å to H bond to heme propionate D. Although the 2Fo-Fc map contoured at 1.0σ reveals density for the second aminopyridine group, the B factors for this group are relatively high in comparison with the rest of the molecule, indicating less specific binding of the second aminopyridine group. As modeled, the amine on the second aminopyridine group is positioned within 3.1 Å of Asp220 for a potential H bond (Fig. 3*A*). The second aminopyridine is also modeled as binding within a van der Waals contact radii of Tyr357. The cofactor H_4B also is present in the bsNOS-**1** crystal structure and is bound at the previously characterized bacterial pterin site (16, 17).

Although **2** binds to Glu243 in a near-identical orientation and position as **1**, the second aminopyridine group of **2** displaces the H_4B molecule to form two stabilizing H bonds (2.8 Å and 2.9 Å) with heme propionate A (Fig. 3*B*). Unlike **1**, the electron density for **2** is well defined for the entire inhibitor. The improved electron density corresponds to a lower K_S for **2**, 1.05 μM, compared with **1**, 4.44 μM. (Fig. 3). The binding mode of **2** is further stabilized by the cation–π interaction with the nearby Arg247, a H bond (2.9 Å) between the primary amine and Glu243, and a H bond (3.0 Å) between the primary amine and the heme propionate A (Fig. 2*B*).

Comparisons with nNOS and eNOS. A consistent finding in the bsNOS inhibitor crystal structures is the presence of a large solvent molecule located where the carboxyl group of the substrate, L-Arg, would be located. Modeling a Cl^- anion at this position accounts best for the electron density. In the eNOS-**2** structure, there is an acetate ion located in approximately the same position. Electrostatic stabilization results from the nearby Arg254 and Arg132, both of which are conserved in eNOS and bsNOS (Fig. 3). However, nNOS has no anion at this position (Fig. 3*D*). This is very likely because bsNOS Asn248 (also Asn in eNOS) is replaced with Asp in nNOS. Asn248 is about 3.2 Å from the Cl^- anion, so an Asp at this position would result in weaker electrostatic stabilization of an anion.

The structures of **2** bound to eNOS and nNOS have been determined (18) but not to **1**, so we also determined the crystal structure of the nNOS-**1** complex (Fig. 3*C*). There are two major differences. First, the pyrrolidine ring in nNOS points "up"

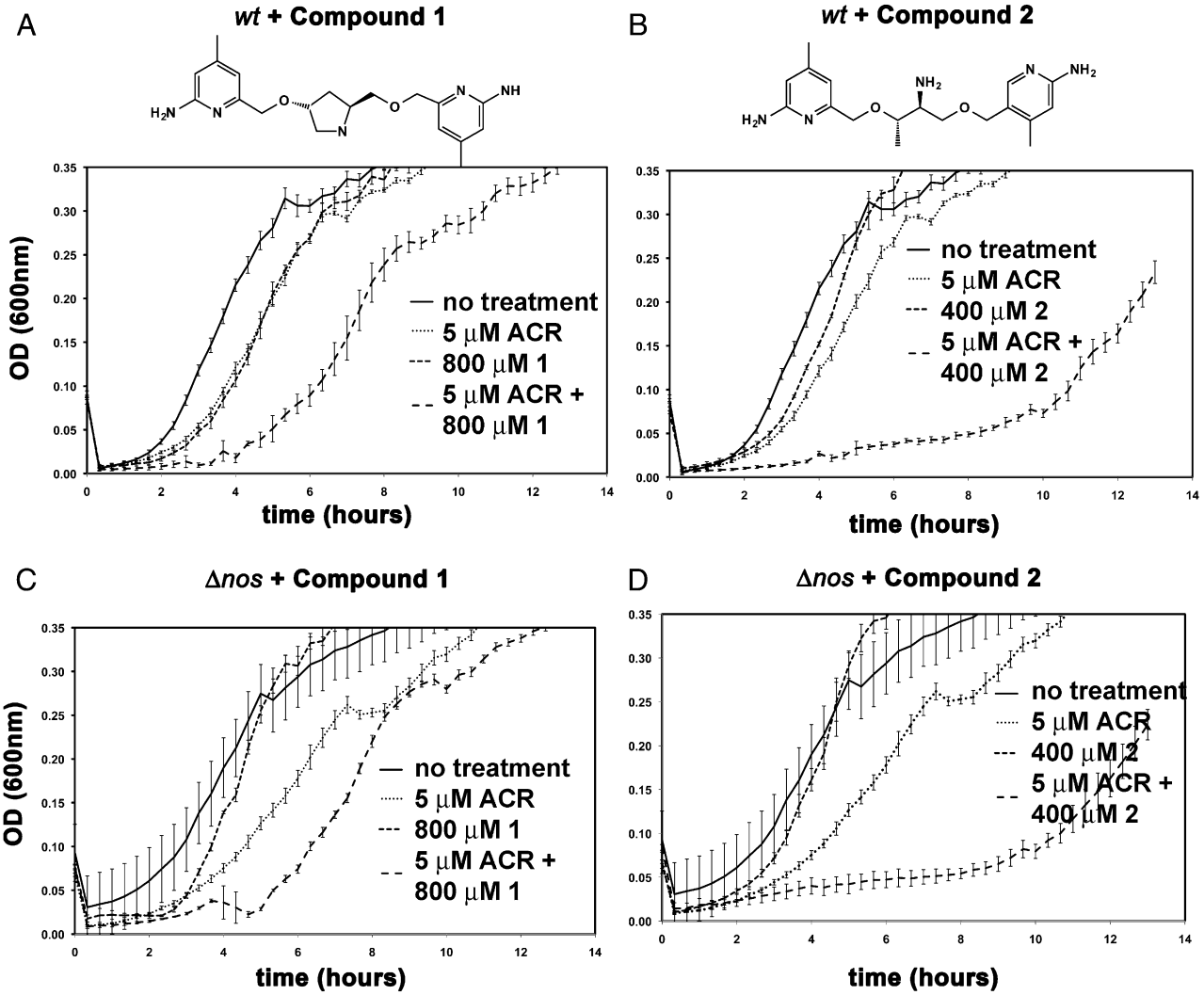

Fig. 2. The effect of ACR and compounds **1** and **2** on bacterial growth in both WT and *Δnos B. subtilis*: (*A*) WT + compound **1**, (*B*) WT + compound **2**, (*C*) *Δnos* + compound **1**, and (*D*) *Δnos* + compound **2**. Error bars represent the mean ± the SEM of three replicates.

toward Asp597, whereas in bNOS, the pyrrolidine ring points "down" toward heme propionate D. Second, Tyr706 is displaced in nNOS, which allows the second aminopyridine to H bond with heme propionate D. Normally, this tyrosine H bonds with heme propionate D, but we have observed in other double-headed NOS inhibitors that this tyrosine readily moves to enable inhibitors to H bond with heme propionate D, which happens more often in nNOS than eNOS (7). We also determined the structure of the eNOS-**1** complex (*SI Appendix*, Fig. S3), and the main difference is that Tyr477 (corresponds to Tyr706 in nNOS) is not displaced. It, therefore, appears that Tyr706 is able to move more freely in nNOS than either eNOS or bsNOS. There are substantial sequence differences between NOS isoforms near Tyr706, but, unfortunately, several residues in this region are not well resolved in nNOS and eNOS electron density maps, so it is difficult to provide a structural basis for the observed enhanced susceptibility of Tyr706 to be displaced in nNOS.

Table 1. Comparison of calculated K_S values at NOS active sites for L-Arg, 1, and 2

Ligand	bsNOS	eNOS	nNOS
L-Arg-1 K_S, μM	0.8	1.0*	0.7†
L-NNA 1 K_S, μM	1.3	0.1‡	0.04†
Compound **1** K_S, μM	4.4	2.1	0.1
Compound **2** K_S, μM	1.1	1.7	0.4

The calculated K_S values were derived from the measured $K_{S,app}$ values. Experiments were performed as described in *Materials and Methods*.
*Data from ref. 29.
†Data from ref. 27.
‡Data from ref. 37.

Fig. 3*D* shows the nNOS-**2** complex. Here there is an even more dramatic difference. Relative to bsNOS, the inhibitor flips 180° in nNOS so that the aminopyridine that is situated near the active site Glu in bsNOS H bonds with heme propionate D in nNOS, which requires movement of Tyr706. This enables the primary amino group in nNOS to H bond with heme propionate D. We attribute this large difference in binding mode of **2** to the displacement of the H_4B cofactor in bsNOS but not in nNOS. The actual physiological cofactor in bsNOS remains an open question, but the binding of pterins to bsNOS is fairly weak, in the 10- to 20-μM range (19), compared with mNOS, which is in the nanomolar range (20). Therefore, H_4B is more easily displaced in bsNOS than in mNOS. As a result, inhibitors targeting the pterin binding pocket might be selective to bsNOS over mNOS.

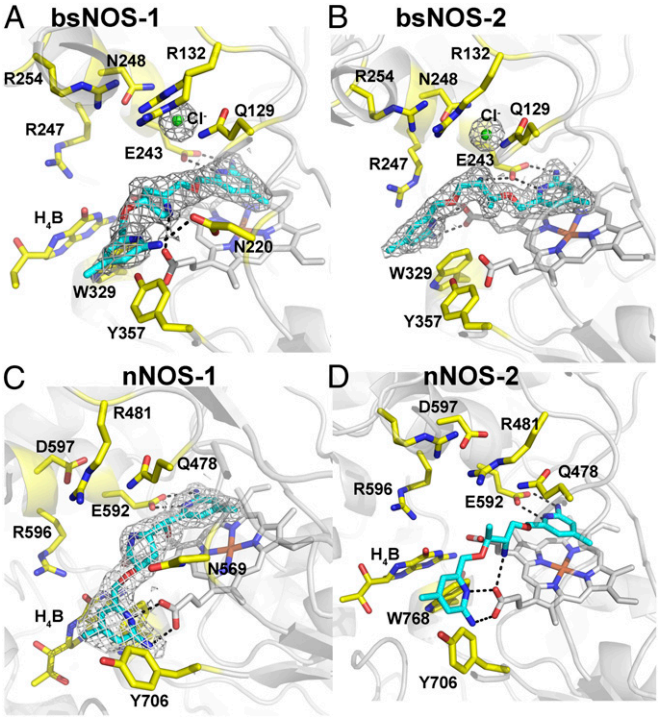

Fig. 3. Active site structure of (*A*) bsNOS-**1** complex with $2F_0$-F_c electron density map contoured at 1.0σ, (*B*) bsNOS-**2** complex with $2F_0$-F_c electron density contoured at 1.0σ, (*C*) *Rattus norvegicus* nNOS-**1** complex with the 2Fo-Fc electron density map contoured at 1.0σ, and (*D*) nNOS-**2** complex.

Conclusions

Although a previous study demonstrated a nonselective NOS inhibitor to render *B. anthracis* more susceptible to H_2O_2 induced oxidative stress (13), this study illustrates the potential of NOS inhibitors to increase the killing efficacy of an antimicrobial. Of the limited number of NOS inhibitors we initially screened, it is interesting that all compounds evaluated bind to bsNOS based on the measured K_s value but only two compounds were found to inhibit bacterial growth. Therefore, there is only a weak correlation between the ability to bind to bsNOS and to enhance the effect of antibiotic-induced oxidative stress in blocking bacterial survival. One explanation for this is the better bioavailability of **1** and **2** relative to the other inhibitors we tested, although we cannot eliminate the possibility that these inhibitors affect bacterial growth by some other mechanism than by inhibiting bsNOS. The most important structural finding is that **2** is able to displace the H_4B cofactor in bsNOS but not mNOS. This observation therefore focuses attention toward the pterin site for future structure-based inhibitor design targeting bNOS.

Materials and Methods

Bacterial Strains. *B. subtilis* 168 was obtained from American Type Culture Collection (23857) and made competent by the Spizizen method (21). NOS deletion vector, pTPJH046, was synthesized by Genscript to contain a spectinomycin resistance gene, adapted from pDG1728 (22), flanked by two 400 BP fragments upstream and downstream of *nos* (*yflM*). *B. subtilis Δnos* was engineered by transforming pTPJH046 and selecting for spectinomycin resistance, as previously reported (11). Double recombination was checked by colony PCR. Spectinomycin was used at 100 μg/mL.

Effect of Oxidative Stress and NOS Inhibitor on *B. subtilis*. *B. subtilis* WT and *Δnos* were grown to an $OD_{600} \approx 1.0$ and diluted to $OD_{600} = 0.6$. Cell stocks were treated with either nonselective NOS inhibitor N^{ω}-nitro-L-arginine (L-NNA), compound **1**, or compound **2** at 500 μM, 500 μM, and 250 μM, respectively, and either H_2O_2 or ACR at 2 mM and 1.25 mM, respectively, for 30 min at 30 °C. Cells were serially diluted in M9 minimal media and plated on LB agar (with 0.5% glucose), and plates were incubated overnight at 37 °C. Colony-forming units were counted the following day and percent survival was calculated. For the *B. subtilis* growth assays, WT and *Δnos* strains were grown in LB media to an $OD_{600} \approx 1.0$ and diluted into LB media until $OD_{600} = 0.28$. The $OD_{600} = 0.28$ cell stocks were then diluted 30-fold into a 96-well plate containing fresh LB media. Cells were pretreated with NOS inhibitors **1** and **2** for 5 min, at 800 μM and 400 μM, respectively. ACR then was added to a final concentration of 5 μM, and growth was monitored at 600 nm for 14 h at 28 °C using a plate reader.

Table 2. Data collection, processing, and refinement statistics of the NOS inhibitor-bound structures

PDB code	bsNOS-1 4LWB	bsNOS-2 4LWA	eNOS-1 4LUW	nNOS-1 4LUX
Data Collection				
Space group	$P2_12_12$	$P2_12_12$	$P2_12_12_1$	$P2_12_12_1$
Cell dimensions *a, b, c*; Å	80.3, 95.1, 62.7	80.6, 95.0, 63.0	58.1, 106.6, 156.8	51.8, 110.9, 164.7
Resolution, Å	50–2.15 (2.19–2.15)	50–2.06 (2.1–2.06)	50–2.25 (2.29–2.25)	50–1.86 (1.89–1.86)
R_{merge}	0.133 (0.581)	0.076 (0.259)	0.069 (0.613)	0.066 (0.581)
$I/\sigma I$	17.9 (2.3)	26.5 (3.8)	19.4 (1.9)	24.2 (1.7)
Completeness, %	99.55 (99.02)	99.49 (95.48)	98.92 (96.90)	99.23 (98.82)
Redundancy	5.6 (3.9)	5.4 (4.5)	3.6 (3.5)	4.0 (4.0)
Refinement				
Resolution, Å	43.86–2.15	49.66–2.05	44.07–2.25	39.01–1.86
No. of reflections	26,851	29,233	46,580	80,292
R_{work}/R_{free}	0.185 (0.281)/0.233 (0.318)	0.168 (0.196)/0.202 (0.225)	0.184 (0.295)/0.233 (0.331)	0.180 (0.315)/0.212(0.362)
No. of atoms	3,249	3,283	6,941	7,326
Protein	2,957	2,949	6,438	6,682
Ligand/ion	93	75	207	181
Water	199	259	296	463
B factors				
Protein	43.3	32.2	44.2	40.7
Ligand/ion	48.9	32.5	44.5	33.3
Water	43.2	38.1	27.2	27.6
rms deviations				
Bond lengths, Å	0.012	0.013	0.016	0.015
Bond angles, °	2.04	2.03	1.62	1.45

Values in parentheses are for highest-resolution shell.

Cloning and Mutagenesis. The *B. subtilis* NOS sequence was obtained from GenBank (23). The DNA sequence was codon optimized for bacterial expression, synthesized, and cloned into a pET28a vector (Novagen) using the NdeI and XhoI restriction sites by GenScript. Site-directed mutagenesis was carried out using the QuikChange Lightning Site-Directed Mutagenesis Kit (Stratagene) to introduce surface mutations E25A/E26A/E316A.

Protein Expression and Purification. *B. subtilis* NOS (bsNOS) was expressed and purified as previously reported (16). Heme domains of nNOS and eNOS were also expressed and purified as previously reported (24, 25).

Imidazole Displacement. Coordination of imidazole to the heme iron generates a low spin spectrum with a Soret peak at 430 nm. NOS inhibitors displace the imidazole ligand and shift the heme to high spin, resulting in a Soret maximum at 395 nm. This provides a convenient method for estimating the spectral dissociation constant, K_s (26, 27). High spin ligands were titrated into a cuvette containing 2 μM NOS, 1 mM imidazole, 50 mM Tris pH 7.6, and 100 μM DTT. An apparent K_s ($K_{s,app}$) was calculated based on a nonlinear regression analysis using Sigmaplot version 10.0 (Systat Software, Inc., www.sigmaplot.com) using Eq. **1**, $A_{395} - A_{430} = \frac{B_{max} \cdot [I]}{K_{s,app} + [I]}$. Assuming K_d of imidazole for bsNOS to be 384 μM (28), for nNOS to be 160 μM (15), and for eNOS to be 150 μM (29), the K_S was calculated as previously reported (27).

Crystallization. Crystals of bsNOS belonging to space group $P2_12_12$ were grown by vapor diffusion at 22 °C. Initial crystals were obtained by mixing an equal volume of the crystallization reservoir and bsNOS at 25 mg/mL in 25 mM Tris pH 7.6, 150 mM NaCl, 1 mM DTT. The reservoir was composed of 60 mM Bis-Tris methane/40 mM citric acid pH 7.6 and 20% (vol/vol) polyethylene glycol (PEG) 3350. Crystal quality was further improved by introduction of surface entropy mutants E25A/E26A/E316A identified using the Surface Entropy Reduction Prediction (sERP) server (30). Each glutamate was selected for mutation as a residue predicted to facilitate crystal packing (31) and as a residue that did not contribute a stabilizing noncovalent interaction with nearby residues. Crystals of the E25A/E26A/E316A bsNOS were then seeded into an equal volume drop of reservoir containing 60 mM Bis-Tris methane/40 mM citric acid pH 7.6, 15% (vol/vol) PEG 3350, 1.9% (vol/vol) 1-propanol and protein containing E25A/E26A/E316A bsNOS at 18 mg/mL in 25 mM Bis-Tris methane pH 7.6, 150 mM NaCl, 1% (vol/vol) glycerol, 1% (wt/vol) PEG 3350, 1 mM DTT, and 500 μM imidazole. Enzyme inhibitor H_4B complex crystals were prepared during the cryoprotection with 23% (vol/vol) glycerol by soaking at inhibitor and H_4B concentrations of 7–10 mM and 2 mM, respectively, for 3–6 h. The heme domain of eNOS and nNOS were prepared and crystallized as described (24, 25).

Data Collection and Structure Determination. High-resolution data were collected at the Stanford Synchrotron Radiation Lightsource (SSRL) beamline 7–1. Data frames were indexed, integrated, and scaled using HKL2000 (32). Phases were determined by molecular replacement using Phaser (33) with the PDB entry 2FBZ as the search model for bsNOS inhibitor-bound structures. Inhibitor topology files were constructed using the online program PRODRG (34); protein and inhibitor were modeled in Coot (35) and refined using REFMAC (36). Water molecules were added and checked by REFMAC and COOT, respectively. Crystallographic data collection and refinement statistics are listed in Table 2.

Chemical Synthesis. Details of the synthesis of compounds **1** and **10** are provided in *SI Appendix*.

ACKNOWLEDGMENTS. We thank Dr. Manuela Raffatellu and Dr. Yilin Hu for illuminating discussions on engineering a *B. subtilis Δnos* strain and experimental design. We also thank the beamline staff at Stanford Synchrotron Radiation Laboratory and Advanced Light Source for their assistance during the remote X-ray diffraction data collections. This work was supported by National Institutes of Health Grants GM57353 (to T.L.P.) and GM49725 (to R.B.S.).

1. Sudhamsu J, Crane BR (2009) Bacterial nitric oxide synthases: What are they good for? *Trends Microbiol* 17(5):212–218.
2. Moncada S, Palmer RM, Higgs EA (1991) Nitric oxide: Physiology, pathophysiology, and pharmacology. *Pharmacol Rev* 43(2):109–142.
3. Alderton WK, Cooper CE, Knowles RG (2001) Nitric oxide synthases: Structure, function and inhibition. *Biochem J* 357(Pt 3):593–615.
4. Griffith OW, Stuehr DJ (1995) Nitric oxide synthases: Properties and catalytic mechanism. *Annu Rev Physiol* 57:707–736.
5. Calabrese V, et al. (2007) Nitric oxide in the central nervous system: Neuroprotection versus neurotoxicity. *Nat Rev Neurosci* 8(10):766–775.
6. Silverman RB (2009) Design of selective neuronal nitric oxide synthase inhibitors for the prevention and treatment of neurodegenerative diseases. *Acc Chem Res* 42(3): 439–451.
7. Poulos TL, Li H (2013) Structural basis for isoform-selective inhibition in nitric oxide synthase. *Acc Chem Res* 46(2):390–398.
8. Buddha MR, Tao T, Parry RJ, Crane BR (2004) Regioselective nitration of tryptophan by a complex between bacterial nitric-oxide synthase and tryptophanyl-tRNA synthetase. *J Biol Chem* 279(48):49567–49570.
9. Kers JA, et al. (2004) Nitration of a peptide phytotoxin by bacterial nitric oxide synthase. *Nature* 429(6987):79–82.
10. Gusarov I, et al. (2013) Bacterial nitric oxide extends the lifespan of *C. elegans*. *Cell* 152(4):818–830.
11. Gusarov I, Nudler E (2005) NO-mediated cytoprotection: Instant adaptation to oxidative stress in bacteria. *Proc Natl Acad Sci USA* 102(39):13855–13860.
12. Gusarov I, Shatalin K, Starodubtseva M, Nudler E (2009) Endogenous nitric oxide protects bacteria against a wide spectrum of antibiotics. *Science* 325(5946):1380–1384.
13. Shatalin K, et al. (2008) Bacillus anthracis-derived nitric oxide is essential for pathogen virulence and survival in macrophages. *Proc Natl Acad Sci USA* 105(3):1009–1013.
14. Kohanski MA, Dwyer DJ, Hayete B, Lawrence CA, Collins JJ (2007) A common mechanism of cellular death induced by bactericidal antibiotics. *Cell* 130(5):797–810.
15. McMillan K, Masters BS (1993) Optical difference spectrophotometry as a probe of rat brain nitric oxide synthase heme-substrate interaction. *Biochemistry* 32(38):9875–9880.
16. Pant K, Bilwes AM, Adak S, Stuehr DJ, Crane BR (2002) Structure of a nitric oxide synthase heme protein from *Bacillus subtilis*. *Biochemistry* 41(37):11071–11079.
17. Bird LE, et al. (2002) Crystal structure of SANOS, a bacterial nitric oxide synthase oxygenase protein from *Staphylococcus aureus*. *Structure* 10(12):1687–1696.
18. Jing Q, et al. (2013) Chiral linkers to improve selectivity of double-headed neuronal nitric oxide synthase inhibitors. *Bioorg Med Chem* 23(20):5674–5679.
19. Crane BR, Sudhamsu J, Patel BA (2010) Bacterial nitric oxide synthases. *Annu Rev Biochem* 79:445–470.
20. Tejero J, Stuehr D (2013) Tetrahydrobiopterin in nitric oxide synthase. *IUBMB Life* 65(4):358–365.
21. Anagnostopoulos C, Spizizen J (1961) Requirements for transformation in *Bacillus subtilis*. *J Bacteriol* 81(5):741–746.
22. Guérout-Fleury AM, Frandsen N, Stragier P (1996) Plasmids for ectopic integration in *Bacillus subtilis*. *Gene* 180(1-2):57–61.
23. Kunst F, et al. (1997) The complete genome sequence of the gram-positive bacterium *Bacillus subtilis*. *Nature* 390(6657):249–256.
24. Li H, et al. (2002) The novel binding mode of N-alkyl-N′-hydroxyguanidine to neuronal nitric oxide synthase provides mechanistic insights into NO biosynthesis. *Biochemistry* 41(47):13868–13875.
25. Raman CS, et al. (1998) Crystal structure of constitutive endothelial nitric oxide synthase: A paradigm for pterin function involving a novel metal center. *Cell* 95(7): 939–950.
26. Salard-Arnaud I, Stuehr D, Boucher JL, Mansuy D (2012) Spectroscopic, catalytic and binding properties of Bacillus subtilis NO synthase-like protein: Comparison with other bacterial and mammalian NO synthases. *J Inorg Biochem* 106(1):164–171.
27. Roman LJ, et al. (1995) High-level expression of functional rat neuronal nitric oxide synthase in *Escherichia coli*. *Proc Natl Acad Sci USA* 92(18):8428–8432.
28. Wang ZQ, et al. (2004) A conserved Val to Ile switch near the heme pocket of animal and bacterial nitric-oxide synthases helps determine their distinct catalytic profiles. *J Biol Chem* 279(18):19018–19025.
29. Berka V, Chen PF, Tsai AL (1996) Spatial relationship between L-arginine and heme binding sites of endothelial nitric-oxide synthase. *J Biol Chem* 271(52):33293–33300.
30. Goldschmidt L, Cooper DR, Derewenda ZS, Eisenberg D (2007) Toward rational protein crystallization: A Web server for the design of crystallizable protein variants. *Protein Sci* 16(8):1569–1576.
31. Derewenda ZS (2004) Rational protein crystallization by mutational surface engineering. *Structure* 12(4):529–535.
32. Otwinowski Z, Minor W (1997) Processing of X-ray diffraction data collected in oscillation mode. *Methods Enzymol* 276:307–326.
33. McCoy AJ, et al. (2007) Phaser crystallographic software. *J Appl Cryst* 40(Pt 4):658–674.
34. Schüttelkopf AW, van Aalten DM (2004) PRODRG: A tool for high-throughput crystallography of protein-ligand complexes. *Acta Crystallogr D Biol Crystallogr* 60(Pt 8): 1355–1363.
35. Emsley P, Lohkamp B, Scott WG, Cowtan K (2010) Features and development of Coot. *Acta Crystallogr D Biol Crystallogr* 66(Pt 4):486–501.
36. Murshudov GN, Vagin AA, Dodson EJ (1997) Refinement of macromolecular structures by the maximum-likelihood method. *Acta Crystallogr D Biol Crystallogr* 53(Pt 3): 240–255.
37. Martasek P, et al. (1996) Characterization of bovine endothelial nitric oxide synthase expressed in *E. coli*. *Biochem Biophys Res Commun* 219(2):359–365.